PNAS RESEARCH ARTICLE | CHEMISTRY

Crystalline $C_3N_3H_3$ tube (3,0) nanothreads

Dexiang Gao[a,1], Xingyu Tang[a,1], Jingqin Xu[a], Xin Yang[a], Peijie Zhang[a], Guangwei Che[a], Yajie Wang[a], Yongjin Chen[a], Xiang Gao[a], Xiao Dong[b], Haiyan Zheng[a,2], Kuo Li[a], and Ho-kwang Mao[a,2]

HPSTAR 1612-2022

Contributed by Ho-kwang Mao; received January 25, 2022; accepted March 9, 2022; reviewed by Malcolm Guthrie, Yan Li, and Bingbing Liu

Carbon nanothread (CNTh) is a "one-dimensional diamond polymer" that combines high tensile strength and flexibility, but it severely suffers from intrathread disorder. Here, by modifying the reactivity and the stacking ordering of the aromatic precursor, crystalline $C_3N_3H_3$ CNTh with perfect hexagonal orientation and stacking was synthesized at 10.2 GPa and 573 K from *s*-triazine. By Rietveld refinement of X-ray diffraction data, gas chromatography mass spectrometry investigation, and theoretical calculation, we found that synthesized CNTh has a tube (3,0) structure, with the repeating *s*-triazine residue connected solely by C–N bonds along the thread. A "pericage" reaction, the concerted bonding between six C and N atoms, instead of [4 + 2] or [1,4] addition reactions, was concluded for the formation of CNThs, and the critical bonding distance between the nearest intermolecular C and N was ∼2.9 Å. The formation of a "structure-specific" crystalline CNTh with C and N orderly distributed highlighted the importance of reaction selectivity and stacking order of reactant molecules, which have great significance for understanding the polymerization of aromatic molecules under high pressure and developing new crystalline CNThs.

crystalline nanothread | triazine | tube (3,0) | concerted [1,3,5] addition reaction | pressure-induced polymerization

Significance

The diamond nanothread is predicted to have comparable or larger strength and stiffness than the carbon nanotube but severely suffers from intrathread bonding disorder in practice. Here, we synthesized a bulk crystalline diamond nanothread material $C_3N_3H_3$ with a C/N-ordered tube (3,0) structure via high-pressure topochemical polymerization of *s*-triazine. The π-stacked *s*-triazine experienced a selective concerted bonding of three neighbored C···N pairs, completely different from the classical Diels–Alder reactions of aromatics under high pressure. This study obtained the structure-specific diamond nanothread with an unambiguous elemental reaction, which is the basis to realize the expected excellent properties of diamond nanothreads. Following the identified reaction selectivity under high pressure, more structure-specific carbon materials can be designed.

sp^3-Carbon nanothreads (CNThs; diamond nanothread) have attracted significant attention due to their extremely high strength, flexibility, and resilience since the first report in 2015 (1–3). CNTh was typically synthesized by pressure-induced polymerization (PIP) of aromatics, such as benzene, pyridine, furan, etc. (3–15), through which the π electrons bond to form σ bonds approximately along the threads. However, the new bonds are often not in good order, and the crystallinity of these CNThs is hence not satisfying. Typically, only the first-order diffraction of a pseudohexagonal lattice was detected at $d = 5$ to 6 Å, suggesting a pseudohexagonal stacking of the CNThs along the *c* axis. The intrathread structure and the orientation of the CNThs on the *a*-*b* plane were disordered or unknown, which affected its physical and chemical properties and further development.

Precise synthesis of intrathread-ordered or even structure-specific CNThs relies on the reaction selectivity of the monomers, which again depends on the reactivity of the composed atoms and the stacking of the molecules under high pressure. To control the stacking, the strong intermolecular interaction between aryl and perfluoroaryl groups was used to construct alternately stacked cocrystals, and, therefore, H, F alternately modified CNThs were obtained (6–8). This strategy was partly successful in regulating the direction of bonding and hence improved the interthread order, but the intrathread bonding was still unknown or controversial (6, 7). Sometimes the product is not CNTh but two-dimensional (2D) H, F graphane materials (16). This is likely due to the similar reactivity of the carbon atoms, which results in diverse and complex bonding during PIP. For example, in benzene (Scheme 1*A*) the reactivities of the six carbon atoms are the same, and both Diels–Alder and 1,1′ coupling reactions are possible; hence, there are many reaction pathways and subsequent reactions, which would destroy the intrathread ordering (17). The second strategy is to modify the atoms on the aromatic ring to improve its reaction selectivity. In PIP of furan and thiophene, the Diels–Alder reaction of the carbon atoms was promoted because O and S atoms are inert to addition reactions (12, 13). However, there are still exo/endo pathways, which produce *anti*- or *syn*-connected five-member rings (12, 13) (Scheme 1*B*). Such diverse connection induces intrathread and interthread stress, which also destroys the interthread ordering upon decompression.

Based on the above knowledge, we need to improve the reaction selectivity on the aromatic ring and their stacking order simultaneously (Scheme 1*C*). Compared to carbon, unsaturated nitrogen is very inert in such addition reactions, because the bonding energy of N=N is bigger than two N–N single bonds. Practically, acetylene polymerizes at 5.7 GPa, while the isoelectronic molecule N_2 polymerizes above 100 GPa (18, 19). In the PIP of tetrazole, only the C–N bond, rather than N–N bond, formed (20). *s*-Triazine ($C_3N_3H_3$) has alternate C/N arrangement on the ring and perfect π–π stacking in

Author contributions: H.Z., K.L., and H.M. designed research; D.G. performed research; X.T., J.X., X.Y., P.Z., G.C., Y.W., Y.C., X.G., and X.D. contributed new reagents/analytic tools; and D.G. wrote the paper.

Reviewers: M.G., Oak Ridge National Laboratory Neutron Sciences Directorate; Y.L., Peking University; and B.L., Jilin University.

The authors declare no competing interest.

[1]D.G. and X.T. contributed equally to this work.

[2]To whom correspondence may be addressed. Email: zhenghy@hpstar.ac.cn or maohk@hpstar.ac.cn.

This article contains supporting information online at http://www.pnas.org/lookup/suppl/doi:10.1073/pnas.2201165119/-/DCSupplemental.

Published April 19, 2022.

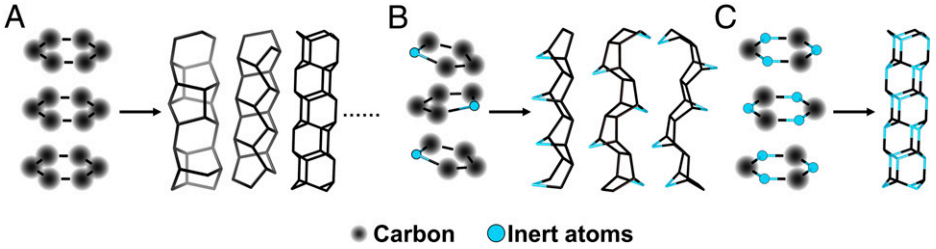

Scheme 1. Effects of reaction selectivity on the formation of CNThs from unsaturated molecules in the crystal. The bonding between carbon and carbon is easier than inert–inert atoms, hence allowing many bonding routes (*A*). Introducing inert atoms can help to improve the reaction selectivity (*B*), and CNTh with a specific structure can be obtained if the modified molecules are also in suitable crystal structure (*C*).

rhombohedrally arranged columns perpendicular to the molecular plane (21). The N atoms are right against the C atoms of the neighbored *s*-triazine, which turned out to be important in the reaction selectivity in PIP in this work. *s*-Triazine was reported to experience a slight lattice distortion at 0.6 GPa and polymerize below 8 GPa above 500 K or above 14 GPa at room temperature, but the structure of the product is still unknown (22–24). In this work, we investigated *s*-triazine up to 40 GPa and 573 K and found that it experienced a PIP process. The recovered product is a hexagonally stacked tube (3,0) CNTh with perfect intrathread ordering and uniform azimuthal orientation. The elemental reaction was a concerted bonding between three C atoms and three N atoms from neighbored molecules. Our work reported the formation of stoichiometric and ordered $C_3N_3H_3$ CNTh, clearly explained the mechanism from precursors to CNThs, and uncovered the importance of reaction selectivity on the structural regulation of final products, which have great significance for designing new CNThs and new PIP synthetic routes.

Results and Discussion

We compressed *s*-triazine in diamond anvil cells (DAC), and the in situ powder X-ray diffraction (XRD) started to show new features gradually at main peak and its second order peak at 15.7° above 11 GPa (marked by the asterisks in *SI Appendix*, Fig. S1 and Fig. 1*A*), which is attributed to the PIP according to our in situ Raman and infrared (IR) spectroscopic investigation (*SI Appendix*, Fig. S2 and Table S1) as well as a previous report (25). From 25.9 to 40.9 GPa, only the diffraction peak at 8° (d = 4.4 Å; Fig. 1*A*) was maintained. This is unambiguously assigned to the product, because in the decompression process at 2.8 GPa, this peak shifts to the low-angle side of the

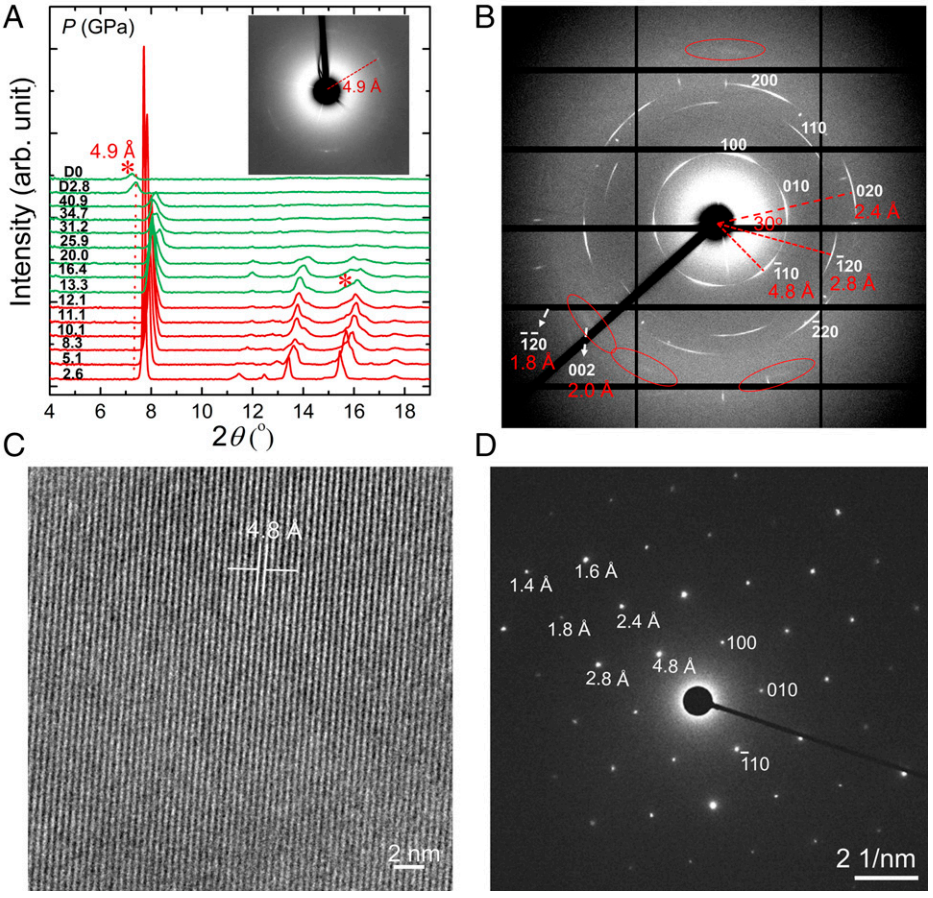

Fig. 1. Crystallographic investigation of *s*-triazine and the recovered products. (*A*) Selected in situ XRD of *s*-triazine up to 40.9 GPa and during decompression at room temperature. The new diffraction peaks from CNThs are marked by the asterisks. (*Inset*) The 2D XRD pattern of RT40. arb., arbitrary. (*B*) XRD pattern and (*C*) HRTEM image of HT10 (recovered from 573 K and 10.2 GPa). (*D*) SAED pattern of the CNThs.

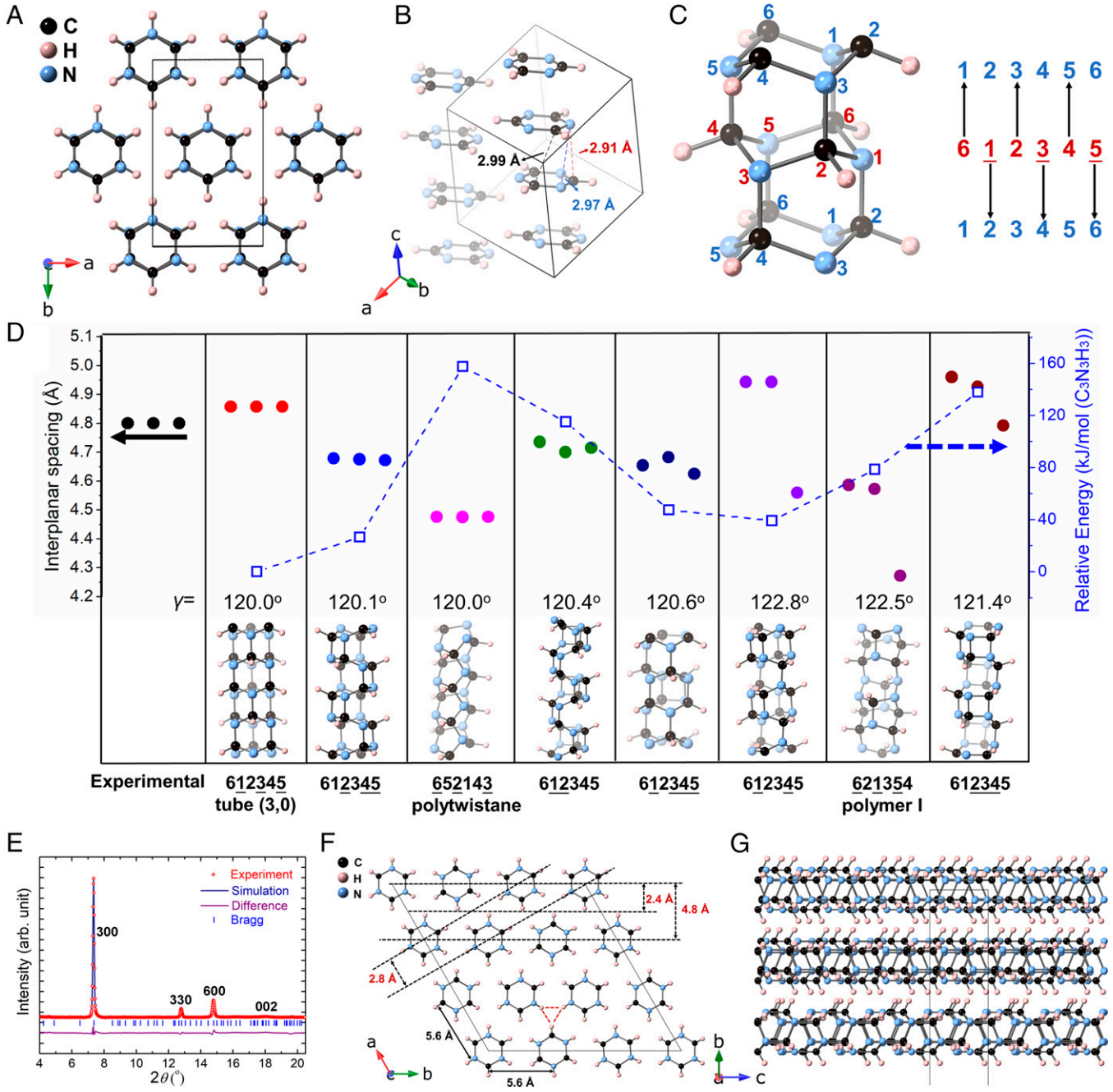

Fig. 2. Structural investigation of CNTh. (*A*) Crystal structure of *s*-triazine at 12.1 GPa. (*B*) The closest intermolecular distances at 12.1 GPa. (*C*) Naming of sp^3 CNThs. The red number is the name of the CNThs. (*D*) {010} *d*-spacings of product HT10 and the {010} *d*-spacings of selected theoretically optimized degree-6 CNTh models in pseudohexagonal stacking. The lattice parameter γ and the relative formation energy [relative to the energy of tube (3,0)] are also presented. (*E*–*G*) Rietveld refinement results of the XRD pattern of product HT10, R_{wp} = 4.73%, and the obtained crystal structure of CNTh as viewed in *F* [001] and *G* [100]. R_{wp}, weighted profile R-factor.

peak at 2.6 GPa in the compression process. When decompressed to ambient pressure, the peak shifts to 4.9 Å, corresponding to the {010} planes of the hexagonal lattice of stacked CNThs ({110} planes of the original R lattice). As shown in the *Inset* of Fig. 1*A*, the 2D XRD image of the product (referred to as RT40) exhibited a hexagonal symmetry. Such a hexagonal pattern with $d = 5$ to 6 Å is what is normally seen for CNTh (4, 8, 10–13) and indicates that the product is also a CNTh. It also suggests that the detected CNTh columns are approximately aligned along the axis of the DAC, which is likely related to the applied uniaxial stress, as discussed in the literature (11, 26, 27).

The crystallinity of the product was improved by heating *s*-triazine to 573 K at 10.2 GPa (pressure and temperature conditions found by in situ Raman spectroscopy under high pressure and high temperature in *SI Appendix*, Fig. S3). The recovered sample (referred to as HT10) showed good crystallinity with five distinctive XRD peaks and the smallest *d*-spacing down to 1.8 Å (Fig. 1*B*). This is in obvious contrast to many CNThs that only show the first-order diffraction at $d \sim 5$ to 6 Å (4, 8, 10–13) and hence suggests a much better ordering. HT10 exhibits precise hexagonal symmetry in the 2D XRD pattern (Fig. 1*B*), so the peaks at 4.8, 2.8, 2.4, and 1.8 Å are indexed as {010}, {110}, {020}, and {120}, respectively, with $a = b$

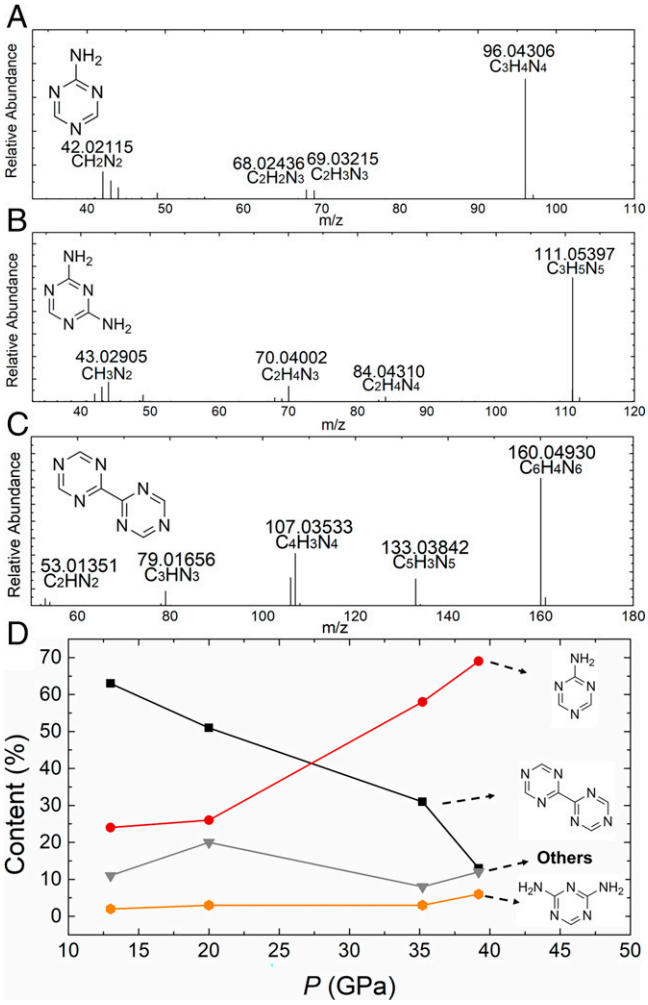

Fig. 3. Mass spectra of the recovered high-pressure product. Mass spectra of $C_3H_4N_4$ (*A*), $C_3H_5N_5$ (*B*), and $C_6H_4N_6$ (*C*) are shown. (*D*) Content evolution of $C_3H_4N_4$, $C_3H_5N_5$, and $C_6H_4N_6$ in the recovered sample of *s*-triazine from 13.0, 20.0, 35.2, and 39.2 GPa.

= 5.6 Å and $\gamma = 120°$. Additionally, a weak diffraction at $d =$ 2.0 Å was observed (red circles in Fig. 1*B*), which corresponds to the half translational period inside the CNTh and hence was indexed as {002} (discussed below). This pattern clearly demonstrates the good ordering of the CNThs' projection on the *a-b* plane, which suggests that the intrathread structure of CNThs (along the *c* axis) should also be homogeneous, while the 002 peak indicates that there is also ordering to some extent along the *c* axis.

High-resolution transmission electron microscopy (HRTEM) images and selected area electron diffraction (SAED) patterns also support the hexagonal stacking of the CNThs with some disorder along the *c* axis (Fig. 1 *C* and *D*). The observed parallel fringes and the morphology of the crystallites (*SI Appendix*, Fig. S4) clearly show the linear structure, and the *d*-spacing of 4.8 Å between the fringes agrees with the strong {010} diffraction in the XRD, corresponding to the distance between adjacent CNTh layers. The sharp SAED spots, even down to $d = 1.4$ Å, are also indexed by the same 2D hexagonal lattice in the *a-b* plane (Fig. 1*D*). For the *c* axis, when the sample was significantly tilted from −13° to 13° continuously, the diffraction spots maintained (*SI Appendix*, Fig. S5), but with the hexagonal lattice deformed and some *d*-spacing decreasing. This clearly suggests that the reciprocal spots extend to rods, and, therefore, the CNThs are disordered to some extent along the *c* axis.

To understand the crystal structure of the product, we need to start from that of the reactant at threshold reaction pressure (12.1 GPa), which was determined by Rietveld refinement of the in situ XRD data, with the plot and the refinement results presented in *SI Appendix*, Fig. S6 and Tables S2 and S3. As indicated in Fig. 2 *A* and *B*, at 12.1 GPa, the π–π stacking of *s*-triazine maintains along the *c* axis, and adjacent molecules are still parallel with C against N and the corresponding distance 2.91 Å. This is close to the critical reaction distance of the aromatic system under high pressure and room temperature, like benzene (2.8 Å) and C_6H_6–C_6F_6 (2.8 Å) etc. (16, 28), which means it is possible for *s*-triazine to polymerize via C···N bonding. In contrast, the closest distance between N atoms of neighbored *s*-triazine is 2.97 Å, too far to induce N–N bonding. For reference, even 2.52 Å is not enough to induce a new N–N bond (20). The closest intermolecular C···C distance is 2.99 Å, a little bit farther than the threshold in the aromatic system (16, 28). Thus, from the topochemical perspective, the most favored bonding is between C and N atoms, which is suitable for forming the tube (3,0) structure as discussed below.

According to previous reports on the intrathread structure of CNTh (17), a series of structures considering new C–N bonds with the degrees of saturation 2, 4, and 6 (the number of saturated C/N atoms per $C_3N_3H_3$ unit) were enumerated and optimized (at most two *s*-triazine per topological unit cell) at ambient pressure (29). The possible structure was named following the literature, and the unbonded atoms are labeled as 0 (Fig. 2*C*) (29). The fully saturated degree-6 CNTh, including tube (3,0), polymer I, polytwistane, and [4 + 2] cycloaddition product followed by a "zipper" reaction, and the partly saturated degree-4 and degree-2 CNThs, like the [4 + 2] cycloaddition product and [1,4] polymerization product etc. proposed in previous works of benzene, were taken into consideration (Fig. 2*D* and *SI Appendix*, Figs. S7 and S8) (4, 17). Only 612345 [tube (3,0)], 612345, and 652143 (polytwistane) exhibit good

Table 1. Composition of *s*-triazine recovered from 20 GPa

Formula	Product	Content in PTV injector, %	Content in S/SL injector, %
$C_6H_4N_6$	*	30	51
$C_5H_4N_4$	1H-purine	36	11
$C_6H_5N_5$	*	20	3
$C_6H_5N_7$	*	14	
$C_3H_4N_4$	1,3,5-triazine-2-amine		26
$C_3H_5N_5$	1,3,5-triazine-2,4-diamine		3
$C_6H_6N_6$	*		4
$C_7H_7N_7$	*		2

*The structures could not be found in the NIST database.

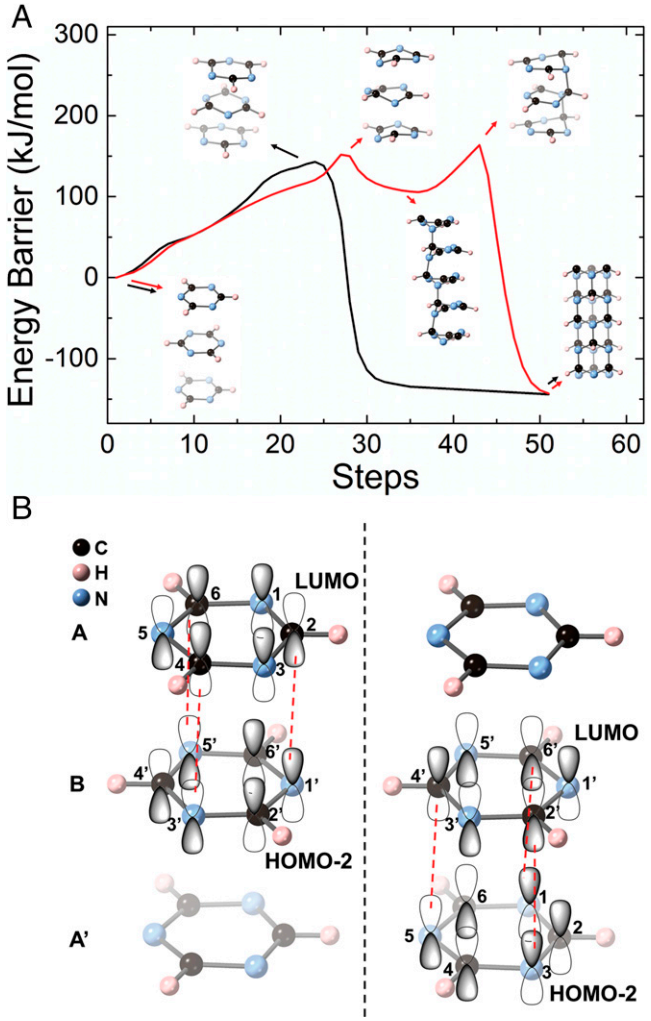

Fig. 4. Theoretical investigation of the addition reaction path of *s*-triazine. (*A*) Enthalpy versus step curves. Red and black lines represent the stepwise and concerted process, respectively. (*B*) Molecular orbitals of *s*-triazine.

(pseudo)hexagonal symmetry, while polymer I and other CNThs have distorted hexagonal lattices (Fig. 2*D* and *SI Appendix*, Figs. S7 and S8). Obviously, the simulated *d*-spacings of tube (3,0) with a perfect hexagonal lattice fit the experimental data best, which indicates that the tube (3,0) is the most possible model of the CNTh. For the polymer with degree of saturation 2 and 4, either [1,2] reaction (610000), [1,4] reaction (600300), or [4 + 2] reaction (650043, $\bar{6}34005$) will cause misalignment and distortion of the CNTh, hence preventing the perfect hexagonal stacking (*SI Appendix*, Fig. S8). We also found that the energy of the tube (3,0) structure is the lowest among all the structures we enumerated. For the CNTh 612345 with similar *d*-spacing, its energy is higher than that of tube $(\bar{3},0)$ by 26 kJ/mol per $C_3N_3H_3$ due to the stress in four-membered rings. According to the energy and the geometric analysis, the tube (3,0) structure should be the most reasonable model of CNTh, which is also supported by the IR spectra of HT10 (*SI Appendix*, Fig. S9) as well as the Rietveld refinement and gas chromatography–mass spectrometry (GC-MS) results shown below.

In the first step, Rietveld refinement was performed to check the orientation of the hexagonal ring on the *a-b* plane. Since most of the XRD peaks of HT10 are indexed as (hk0), which are only affected by the atomic coordinates on the *a-b* plane, a unit cell with $a = b = 5.6$ Å, $\alpha = \beta = 90°$, $\gamma = 120°$, and space group *P*1 was selected; *c* was set to 0.1 Å to avoid any interference of hkl (l≠0) peak. Because the projection of tube (3,0)'s intersection on the *a-b* plane is exactly an ideal quasihexagonal *s*-triazine molecule, four independent *s*-triazine molecules were restrained as rigid bodies on the *a-b* plane with their centers on the 00*c* axis to simulate the projection of tube (3,0) on the *a-b* plane, and only the azimuthal angles were refined to check the orientational ordering. The refinement always converged with all the projections of molecules on the *a-b* plane approximately overlapping each other, forming a hexagon instead of a quasi-circle, fully fitting the projection of intrathread-ordered tube (3,0). Additionally, the resulting model had vertex (C–H and N) pointing to the triangular space (edge-to-edge stacking) with R_{wp}= 4.70% (*SI Appendix*, Fig. S10 *A* and *B*), in contrast to that with C–H/N pointing to the center of adjacent molecules on the *a-b* plane (vertex-to-vertex stacking) with R_{wp} = 12.37% (*SI Appendix*, Fig. S10 *C* and *D*). Hence, we conclude that the CNTh has an ordered tube (3,0) structure and very well-ordered edge-to-edge stacking on the *a-b* plane.

In the second step, since the 002 diffraction (corresponding to the *d*-spacing between the *s*-triazine residual) is still distinguishable, we investigated the relative shift between the CNTs along the *c* axis. A (3 × 3) supercell consisting of nine independent tube (3,0) CNTs with $a = b = 16.8$ Å, $c = 4.0$ Å, $\alpha = \beta = 90°$, $\gamma = 120°$, and space group *P*1 was used for refinement (Fig. 2*E*). Each CNTh was restrained as a rigid body in ideal tube (3,0) structure, with the orientation on the *a-b* plane and the shift along the *c* axis refined. The preferred orientation parameter along [00l] was refined to improve the fitting (that without preferred orientation is displayed in *SI Appendix*, Fig. S11 for comparison). The obtained structure is displayed in Fig. 2 *F* and *G*. In the *a-b* plane, CNTs are still in perfect hexagonal symmetry with the edge-to-edge stacking geometry (Fig. 2*F*). Along the *c* axis (Fig. 2*G*), the relative shift between the CNTs is not in obvious order, as the R_{wp} only changed slightly even if the shifts are fixed in different values (*SI Appendix*, Table S4). This is attributed to the weak interactions between the CNTs.

To confirm the polymerization pathway from *s*-triazine to crystalline tube (3,0), we prepared serial products recovered from 13.0, 20.0, 35.2, and 39.0 GPa at room temperature for the GC-MS analysis. Two different injection methods, including the programmed temperature vaporizer (PTV; the inlet heated from 60 °C to 280 °C to avoid decomposition) and the split/splitless (S/SL; the inlet staying at 280 °C) injector, were used for comparison. As shown in Table 1, in the PTV injector, $C_6H_4N_6$, $C_5H_4N_4$, $C_6H_5N_5$, and $C_6H_5N_7$ were observed, while in the S/SL injector, four additional products $C_3H_4N_4$, $C_3H_5N_5$, $C_6H_6N_6$, and $C_7H_7N_7$ were detected. As described above, the temperature performed in the S/SL injector is obviously higher than that in PTV at the inlet. Thus, these additional products should come from the thermolysis fragments of the polymerized *s*-triazine.

By searching in the National Institute of Standards and Technology/Wiley (NIST) standard Library, $C_3H_4N_4$ and $C_3H_5N_5$ were identified as 1,3,5-triazine-2-amine (NH_2-$C_3H_3N_3$) and 1,3,5-triazine-2,4-diamine (NH_2-$C_3H_3N_3$-NH_2), respectively (Fig. 3 *A* and *B* and *SI Appendix*, Fig. S12). This gives solid evidence that *s*-triazine polymerizes through the C–N bonding under high pressure. $C_6H_6N_6$ and $C_7H_7N_7$ could not be found in the database, but the step loss of the HCN groups was observed in their mass spectra (*SI Appendix*, Fig. S13). This is similar with that of triazine and suggests that the polymerized species ($C_6H_6N_6$ dimer) are composed of triazine residual, with C–N bonds instead of C–C and N–N.

Both in PTV and S/SL injectors, $C_6H_4N_6$ was detected and determined as bis-triazinyl with two *s*-triazine units connected by C–C bonding (Fig. 3*C*), suggesting that the C–C bonding between triazine is a side reaction. We compared the content of $C_3H_4N_4$, $C_3N_5H_5$, and $C_6H_4N_6$ in products recovered from different pressures. Upon increasing pressure, the content of $C_6H_4N_6$ (C–C-bonding route) decreases obviously, while that of $C_3H_4N_4$ (C–N-bonding route) increases (Fig. 3*D*). It means that the *s*-triazine prefers to polymerize through C–N bonding under higher pressure rather than through C–C bonding. All these results confirm that the C–N bonding between adjacent *s*-triazine built up the CNTh. This is also reasonable because, from the perspective of topochemistry, the intermolecular C···N distance is the shortest (2.91 Å at 12.1 GPa), as mentioned above.

This reaction selectivity is also clarified by theoretical calculation with the reaction path from the monomer crystal to tube (3,0) described by the nudged elastic band (NEB) calculation at 12 GPa after geometric optimization. As shown in Fig. 4*A* (black line), a concerted [1,3,5] addition reaction with an energy barrier of 143 kJ per mol $C_3N_3H_3$ was identified, which means it is reasonable to obtain the tube (3,0) structure directly from *s*-triazine by forming C–N bonds to N1, N3, and N5 through the bottom side and to C2, C4, and C6 on the top side synchronously. Stepwise reactions are also calculated for reference. An $6\bar{1}0000$ intermediate product was proposed following [1, 2] addition polymerization (Fig. 4*A*, red line). This intermediate would transform into a tube (3,0) structure directly without experiencing an $61\bar{2}300$ intermediate structure (kinetically unstable). According to the enthalpy-to-step curves of the reactions shown in Fig. 4*A*, the stepwise reaction has an extra step and higher energy barriers (152, 163 kJ per mol $C_3N_3H_3$); therefore, the concerted [1,3,5] addition path is preferred.

The symmetry of the molecular orbitals further illustrates why concerted reaction gains the competitive edge. Fig. 4*B* displays the HOMO-2 (HOMO, highest occupied molecular orbital) and lowest unoccupied molecular orbital (LUMO) on three neighboring *s*-triazine molecules along the *c* direction (HOMO to HOMO-1 orbitals occupied by nonbonding electrons, as shown in *SI Appendix*, Fig. S14). According to the frontier orbital theory, due to the orbital symmetry restriction, LUMO on C2, C4, and C6 of molecule A and HOMO-2 on N1′, N3′, and N5′ of molecule B have the same wave function phase; therefore, new bonds can be formed (Fig. 4*B*, *Left*). On the other side of B, when B provides LUMO and A′ provides HOMO-2, nitrogen atoms on molecule A′ and carbon atoms on molecule B tend to bond (Fig. 4*B*, *Right*). This process can extend through the column and, therefore, completes the addition polymerization to form tube (3,0) CNTh. This is an unprecedented three-dimensional symmetry-allowed reaction, and we named it as "peri-cage" reaction, following the famous pericyclic reaction. Distinct from the traditional concerted reaction at ambient pressure, this is a collective process involving more than two molecules due to the column stacking in solid state, although we do not exclude such reactions between two isolated molecules when possible.

Combining the experimental data and theoretical studies, the reaction route from *s*-triazine to crystalline tube (3,0) CNTh is concluded. Compared with CNTs synthesized from PIP of other aromatic molecules, the synthetic condition is not very harsh, but the crystallinity of CNTh is excellent and the reaction routes are straightforward. The most important reason is the very different reactivities between unsaturated N and C. N–N bonding is not favored, while C–C and C–N are acceptable under high pressure, which results in strong selectivity in bonding. The second reason is that the perfect ordered π–π stacking with C facing N makes the reaction proceed along the stacking direction, via which the formation of CNTh tube (3,0) is favored.

Conclusion

In summary, crystalline tube (3,0) CNTh with long-range intrathread order and uniform azimuthal orientation was produced by compressing *s*-triazine under ∼10 GPa and 573 K. By combining the structure analysis at the threshold reaction pressure (12 GPa) and the GC-MS results, we found that the *s*-triazine polymerizes through C–N bonding instead of the N–N and C–C bonding, and the critical C···N distance between adjacent molecules is determined as ∼2.9 Å. In contrast to the [4 + 2] cycloaddition reaction proposed in benzene, *s*-triazine undergoes a concerted [1,3,5] addition reaction between the six C and N atoms along the stacking direction. We synthesized a structure-specific crystalline CNTh with intrathread and interthread azimuthal ordering. The results show that the distinctive reaction selectivity and the regular molecular packing promote the reaction toward the ordered nanothread, which will provide insight to design more structure-specific carbon materials.

Materials and Methods

In Situ High-Pressure Measurements. The powder *s*-triazine (98%, Innochem) used for in situ Raman, IR, and XRD measurements was loaded in DAC in a glove bag to exclude water. Symmetric DAC with a culet of $d = 300$ μm was used for applying pressure. T-301 stainless steel gaskets were preindented to a thickness of 40 μm, and holes with a diameter of 120 μm were drilled in the center of the indentation to serve as the sample chamber. In situ Raman spectra were measured on the Renishaw Raman microscope using a laser of wavelength 532 nm. Resistance heating was used in the in situ high-pressure and high-temperature Raman experiment. In situ IR spectra were collected on a Bruker VERTEX 70v spectrometer with a HYPERION 2000 microscope. Dried KBr was used in in situ IR measurements to reduce sample thickness. A Globar was used as a conventional source. The spectra were collected in transmission mode in the range of 600 to 4,000 cm^{-1} with a resolution of 2 cm^{-1}. No pressure transmitting medium was used for all the above measurements, and pressure was calibrated by measuring the ruby fluorescence (30). In situ high-pressure synchrotron XRD data were collected at 15U1 beamline of the Shanghai Synchrotron Radiation Facility with 2 × 2 $μm^2$ beam size. The wavelength of the incident monochromatic X-ray was 0.6199 Å, and the instrument was calibrated by CeO_2 standard sample. Dioptas software was used to reduce the collected data (31). Jana 2006 was explored to perform the Rietveld refinement of the XRD pattern of *s*-triazine at 12.1 GPa (32). The entire $C_3N_3H_3$ molecule was restrained as rigid body (C–N bond length at 1.2 Å, C–N–C and N–C–N bond angle at 113° and 127°, respectively), and the preferred orientation parameter along the first peak (110) was refined. The refinements of the XRD pattern of HT10 were performed on TOPAS Academic (version 6) software (33). For the Rietveld refinement investigating the orientation of the hexagonal ring on the *a*-*b* plane, the *s*-triazine molecules were restrained as rigid body (*SI Appendix*), and no preferred orientation parameters were applied. For the Rietveld refinement investigating the relative shift, the nanothreads were restrained as rigid body (*SI Appendix*), and preferred orientation parameters along [00l] were refined.

Samples Synthesized under High-Temperature and High-Pressure Conditions and the Characterization of Recovered Samples. The product (HT10) with improved crystallization was synthesized at 10 GPa and 573 K. The DAC with resistance heating was used for the synthesis. HT10 products were preindented to a thickness of 7 μm and used to collect the IR spectra without using KBr. The IR at ambient conditions were collected on a Bruker VERTEX 70v spectrometer with a HYPERION 2000 microscope, and the experimental parameters were the same as those in the in situ IR experiment described above. The XRD measurements of the recovered products were performed on the 4W2 beamline at the Beijing Synchrotron Radiation Facility with 20 × 30 $μm^2$ beam size. The monochromated incident X-ray wavelength was 0.6199 Å. Both the instrument calibration and data reduction were performed by the method as described

above. HRTEM and SAED patterns were recorded on a JEOL F200 under a voltage of 80 kV. GC-MS measurements were performed on a Thermo Scientific Q Exactive GC hybrid quadrupole orbitrap mass spectrometer. The obtained samples in DAC experiments were dissolved in 10 μL of dichloromethane (CH_2Cl_2, high-performance liquid chromatography purity, 99.9%). A TG-1SilMS capillary column (30 m × 0.25 mm inner diameter × 0.25 μm film thickness) was used, and helium (99.999%) was used as a carrier gas with a constant flow rate of 1.0 mL/min. Two different injection methods were used, including S/SL injector (the inlet temperature at 280 °C; splitless) and PTV injector (the inlet temperature increasing from 60 °C to 280 °C at 1 °C/s); 1 μL of sample was injected manually. The GC oven was increased from 60 °C (held for 1 min) to 280 °C at a rate of 5 °C/min, and the temperature of the transfer lines was set at 280 °C. The system was operated with an electron ionization source at 70 eV, with the temperature of the ion source set at 280 °C. Scan spectra were recorded in the range of 33 to 450 *m/z*. The data were acquired using Thermo Scientific TraceFinder 4.0 software.

Density Functional Theory Calculation. Cambridge Sequential Total Energy Package (CASTEP) (34) and Vienna Ab-initio Simulation Package (VASP) (35) were implemented to perform density functional theory (DFT) calculation. Model structures were constructed following the topo-chemical rule and subsequently optimized in CASTEP to get the relative energies. IR spectra were then calculated for reference (36). All calculations by CASTEP were carried out using norm-conserving (37) pseudopotentials. A local density approximation (LDA) exchange correlation functional by Ceperley and Alder, as parameterized by Perdew and Zunger (38), was used. A plane wave basis with an energy cutoff of 990 eV and *K*-points resolution better than 0.05 was adopted. To find out the reaction pathway from *s*-triazine to CNTh, NEB (39) calculation was worked out in VASP. The projector-augmented plane wave (40) method with LDA and plane wave basis with an energy cutoff of 560 eV were set as well as the same *K*-points resolution. The initial states, intermediate product, and tube (3,0) CNTh involved in the calculation were optimized at 12 GPa at first, and the reaction path was searched with the USPEX code using variable-cell NEB (VC-NEB) method (41) under the same pressure. Molecular orbital calculation of *s*-triazine was performed in Gaussian after an optimization at a B3LYP/6-311G** level (42). DFT-D3(BJ) (43) correction was used to take the noncovalent effects into consideration in VASP and Gaussian, while Ortmann–Bechstedt–Schmidt (OBS) van der Waals correction was used in CASTEP (44).

Data Availability. All study data are included in the article and/or *SI Appendix*.

ACKNOWLEDGMENTS. This work was supported by the National Natural Science Foundation of China (Grants 22022101, 21875006, and 21771011). We acknowledge the support of the National Key Research and Development Program of China (2019YFA0708502). In situ high-pressure angle-dispersive XRD experiments were carried out with the support of the 4W2 beamline at Beijing Synchrotron Radiation Facility and the 15U1 beamline at Shanghai Synchrotron Radiation Facility. We thank Dr. Dongliang Yang and Dr. Chengwen Mao for supporting the in situ XRD measurements under high pressure.

Author affiliations: [a]Center for High Pressure Science and Technology Advanced Research, Beijing 100094, People's Republic of China; and [b]Key Laboratory of Weak-Light Nonlinear Photonics, School of Physics, Nankai University, Tianjin 300071, People's Republic of China

1. D. Stojkovic, P. Zhang, V. H. Crespi, Smallest nanotube: Breaking the symmetry of sp^3 bonds in tubular geometries. *Phys. Rev. Lett.* **87**, 125502 (2001).
2. R. E. Roman, K. Kwan, S. W. Cranford, Mechanical properties and defect sensitivity of diamond nanothreads. *Nano Lett.* **15**, 1585–1590 (2015).
3. T. C. Fitzgibbons *et al.*, Benzene-derived carbon nanothreads. *Nat. Mater.* **14**, 43–47 (2015).
4. X. Li *et al.*, Mechanochemical synthesis of carbon nanothread single crystals. *J. Am. Chem. Soc.* **139**, 16343–16349 (2017).
5. S. J. Juhl *et al.*, Local structure and bonding of carbon nanothreads probed by high-resolution transmission electron microscopy. *J. Am. Chem. Soc.* **141**, 6937–6945 (2019).
6. M. D. Ward *et al.*, Controlled single-crystalline polymerization of $C_{10}H_8$·$C_{10}F_8$ under pressure. *Macromolecules* **52**, 7557–7563 (2019).
7. A. Friedrich *et al.*, Pressure-induced polymerization of polycyclic arene-perfluoroarene cocrystals: Single crystal X-ray diffraction studies, reaction kinetics, and design of columnar hydrofluorocarbons. *J. Am. Chem. Soc.* **142**, 18907–18923 (2020).
8. M. C. Gerthoffer *et al.*, 'Sacrificial' supramolecular assembly and pressure-induced polymerization: Toward sequence-defined functionalized nanothreads. *Chem. Sci. (Camb.)* **11**, 11419–11424 (2020).
9. W. S. Tang, T. A. Strobel, Evidence for functionalized carbon nanothreads from π-stacked, para-disubstituted benzenes. *J. Phys. Chem. C* **124**, 25062–25070 (2020).
10. M. M. Nobrega, E. Teixeira-Neto, A. B. Cairns, M. L. A. Temperini, R. Bini, One-dimensional diamondoid polyaniline-like nanothreads from compressed crystal aniline. *Chem. Sci. (Camb.)* **9**, 254–260 (2017).
11. X. Li *et al.*, Carbon nitride nanothread crystals derived from pyridine. *J. Am. Chem. Soc.* **140**, 4969–4972 (2018).
12. S. Huss *et al.*, Scalable synthesis of crystalline one-dimensional carbon nanothreads through modest-pressure polymerization of furan. *ACS Nano* **15**, 4134–4143 (2021).
13. A. Biswas *et al.*, Evidence for orientational order in nanothreads derived from thiophene. *J. Phys. Chem. Lett.* **10**, 7164–7171 (2019).
14. S. Romi, S. Fanetti, F. Alabarse, A. M. Mio, R. Bini, Synthesis of double core chromophore-functionalized nanothreads by compressing azobenzene in a diamond anvil cell. *Chem. Sci. (Camb.)* **12**, 7048–7057 (2021).
15. S. Fanetti, M. Santoro, F. Alabarse, B. Enrico, R. Bini, Modulating the H-bond strength by varying the temperature for the high pressure synthesis of nitrogen rich carbon nanothreads. *Nanoscale* **12**, 5233–5242 (2020).
16. Y. Wang *et al.*, Pressure-induced Diels–Alder reactions in C_6H_6-C_6F_6 cocrystal towards graphane structure. *Angew. Chem. Int. Ed. Engl.* **58**, 1468–1473 (2019).
17. B. Chen *et al.*, Linearly polymerized benzene arrays as intermediates, tracing pathways to carbon nanothreads. *J. Am. Chem. Soc.* **137**, 14373–14386 (2015).
18. J. Sun *et al.*, Pressure-induced polymerization of acetylene: Structure-directed stereoselectivity and a possible route to graphane. *Angew. Chem. Int. Ed. Engl.* **56**, 6553–6557 (2017).
19. A. F. Goncharov, E. Gregoryanz, H. Mao, Z. Liu, R. J. Hemley, Optical evidence for a nonmolecular phase of nitrogen above 150 GPa. *Phys. Rev. Lett.* **85**, 1262–1265 (2000).
20. D. Gao *et al.*, Phase transition and chemical reactivity of ^{1}H-tetrazole under high pressure up to 100 GPa. *Phys. Chem. Chem. Phys.* **23**, 19503–19510 (2021).
21. P. J. Wheatley, The crystal and molecular structure of *s*-triazine. *Acta Crystallogr.* **8**, 224–226 (1955).
22. S. M. Prasad, A. I. M. Rae, A. W. Hewatt, G. S. Pawley, The crystal structure of *s*-triazine at 5 K. *J. Phys. C Solid State Phys.* **14**, 929–931 (1981).
23. S. Li *et al.*, Effect of pressure on heterocyclic compounds: Pyrimidine and *s*-triazine. *J. Chem. Phys.* **141**, 114902 (2014).
24. M. Citroni *et al.*, Structural and electronic competing mechanisms in the formation of amorphous carbon nitride by compressing *s*-triazine. *J. Phys. Chem. C* **119**, 28560–28569 (2015).
25. M. Citroni, S. Fanetti, R. Bini, Pressure and laser-induced reactivity in crystalline *s*-triazine. *J. Phys. Chem. C* **118**, 10284–10290 (2014).
26. J. Dong *et al.*, Decompression-induced diamond formation from graphite sheared under pressure. *Phys. Rev. Lett.* **124**, 065701 (2020).
27. M. Yao *et al.*, Uniaxial-stress-driven transformation in cold compressed glassy carbon. *Appl. Phys. Lett.* **111**, 101901 (2017).
28. L. Ciabini *et al.*, Triggering dynamics of the high-pressure benzene amorphization. *Nat. Mater.* **6**, 39–43 (2007).
29. E. S. Xu, P. E. Lammert, V. H. Crespi, Systematic enumeration of sp^3 nanothreads. *Nano Lett.* **15**, 5124–5130 (2015).
30. H. K. Mao, J. Xu, P. M. Bell, Calibration of the ruby pressure gauge to 800 kbar under quasi-hydrostatic conditions. *J. Geophys. Res.* **91**, 4673–4676 (1986).
31. C. Prescher, V. B. Prakapenka, DIOPTAS: A program for reduction of two-dimensional X-ray diffraction data and data exploration. *High Press. Res.* **35**, 223–230 (2015).
32. V. Petricek, M. Dusek, L. Palatinus, Crystallographic computing system JANA2006: General features. *Z. Kristallogr.* **229**, 345–352 (2014).
33. A. A. Coelho, TOPAS and TOPAS-academic: An optimization program integrating computer algebra and crystallographic objects written in C^{++}. *J. Appl. Cryst.* **51**, 210–218 (2018).
34. S. J. Clark *et al.*, First principles methods using CASTEP. *Z. Kristallogr.* **220**, 567–570 (2005).
35. G. Kresse, J. Furthmüller, Efficient iterative schemes for ab initio total-energy calculations using a plane-wave basis set. *Phys. Rev. B Condens. Matter* **54**, 11169–11186 (1996).
36. S. Baroni, S. de Gironcoli, A. D. Corso, Phonons and related crystal properties from density-functional perturbation theory. *Rev. Mod. Phys.* **73**, 515–562 (2001).
37. D. R. Hamann, M. Schlüter, C. Chiang, Norm-conserving pseudopotentials. *Phys. Rev. Lett.* **43**, 1494–1497 (1979).
38. J. P. Perdew, A. Zunger, Self-interaction correction to density-functional approximations for many-electron systems. *Phys. Rev. B Condens. Matter* **23**, 5048–5079 (1981).
39. H. Jonsson, G. Mills, K. W. Jacobsen, "Nudged elastic band method for finding minimum energy paths of transition" in *Classical and Quantum Dynamics in Condensed Phase Simulations: Proceedings of the International School of Physics* (World Scientific, Singapore, 1997), pp. 385–404.
40. G. Kresse, D. Joubert, From ultrasoft pseudopotentials to the projector augmented-wave method. *Phys. Rev. B Condens. Matter Mater. Phys.* **59**, 1758–1775 (1999).
41. G.R. Qian et al., Variable cell nudged elastic band method for studying solid–solid structural phase transitions. *Comput. Phys. Commun.* **184**, 2111–2118 (2013).
42. M. J. Frisch *et al.*, *Gaussian 09* (Gaussian, Inc., Wallingford, CT, 2009).
43. S. Grimme, S. Ehrlich, L. Goerigk, Effect of the damping function in dispersion corrected density functional theory. *J. Comput. Chem.* **32**, 1456–1465 (2011).
44. F. Ortmann, F. Bechstedt, W. G. Schmidt, Semiempirical van der Waals correction to the density functional description of solids and molecular structures. *Phys. Rev. B Condens. Matter Mater. Phys.* **73**, 205101 (2006).